Variability in a Mixed Layer Ocean Model Driven by Stochastic Atmospheric Forcing

MICHAEL A. ALEXANDER AND CECILE PENLAND

CIRES, University of Colorado, Boulder, Colorado

(Manuscript received 14 August 1995, in final form 16 February 1996)

ABSTRACT

A stochastic model of atmospheric surface conditions, developed from 30 years of data at Ocean Weather Station P in the northeast Pacific, is used to drive a mixed layer model of the upper ocean. The spectral characteristics of anomalies in the four atmospheric variables: air and dewpoint temperature, wind speed and solar radiation, and many ocean features, including the seasonal cycle are reasonably well reproduced in a 500-year model simulation. However, the ocean model slightly underestimates the range of the mean and standard deviation of both temperature and mixed layer depth over the course of the year. The spectrum of the monthly SST anomalies from the model simulation are in close agreement with observations, especially when atmospheric forcing associated with El Niño is included. The spectral characteristics of the midlatitude SST anomalies is consistent with stochastic climate theory proposed by Frankignoul and Hasselmann (1977) for periods up to ~6 months.

Lead/lag correlations and composites indicate a clear connection between the observed SST anomalies in spring and the following fall, as anomalous warm or cold water created in the deep mixed layer during winter/spring remain below the shallow mixed layer in summer and is then reentrained into the surface layer in the following fall and winter. This re-emergence mechanism also occurs in the model but the temperature anomaly pattern is more diffuse and influences the surface layer over a longer period compared with observations.

A detailed analysis of the simulated mixed layer temperature tendency indicates that the anomalous net surface heat flux plays an important role in the growth of SST anomalies throughout the year and is the dominant term during winter. Entrainment of water into the mixed layer from below strongly influences SST anomalies in fall when the mixed layer is relatively shallow and thus has little thermal inertia. Mixed layer depth anomalies are highly correlated with the anomalous surface mechanical mixing in summer and surface buoyancy forcing in winter.

1. Introduction

Recent observational analyses by Deser and Blackmon (1993), Kushnir (1994), Trenberth and Hurrell (1994), and Deser et al. (1996) have found interannual, decadal, and multidecadal variability in the surface layers of both the atmosphere and ocean over the North Atlantic and North Pacific. Several different physical mechanisms have been proposed for the formation of midlatitude sea surface temperature (SST) anomalies including, air–sea feedback and ocean wave propagation (Latif and Barnett 1994), fluctuations in the thermohaline circulation (Weaver and Sarachik 1991; Delworth et al. 1993), and as a remote response to El Niño conditions in the tropical Pacific (Alexander 1992; Jacobs et al. 1994).

In contrast to climate variability resulting from deterministic processes, fluctuations on seasonal to century timescales and longer can result from random forcing of parts of the climate system. For example, Wunsch (1992) showed that a simple integration of white noise (random fluctuations with no preferred periodicities) has rich temporal structure, similar to some observed ocean time series. In a landmark paper, Hasselmann (1976) proposed that climate could be represented by a slow system that integrates white noise or stochastic forcing representing "weather" as a fast system.[1] Like particles undergoing Brownian motion, the slow climate system exhibits random walk behavior, where the variability increases (decreases) with the square of the period (frequency). Variability in a stochastic climate system is unbounded unless processes that provide negative feedbacks are included.

The study by Frankignoul and Hasselmann (1977) was one of the first to apply a stochastic model to the real climate system in a study of midlatitude SST variability. Here, the upper ocean, the slow system, acts to integrate the white noise atmospheric forcing. This forcing represents the passage of atmospheric storms,

Corresponding author address: Dr. Michael A. Alexander, CIRES, Campus Box 449, University of Colorado, Boulder, CO 80309-0449.
E-mail: maa@cdc.noaa.gov

[1] Some preliminary ideas on using stochastic models to represent air–sea interaction and climate fluctuations were discussed by Mitchell (1976).

where the rapid decorrelation time between synoptic events results in a nearly white spectrum in the frequency domain over the evolution timescale of SST anomalies. The system is damped by a linear negative air–sea feedback, which represents the enhanced loss of heat to the atmosphere from anomalous warm waters and vice versa. Frankignoul and Hasselmann tested this paradigm for midlatitude SST anomalies using a simple atmospheric model coupled to a fixed slab ocean, and by estimating the stochastic parameters, the white noise forcing and linear air–sea feedback factor, from data. Both the simple coupled model and the stochastic parameterization showed similar spectral characteristics as the observed SST anomalies: increasing variability with period for periods less than ~1 year and then a flattening of the spectra at longer periods as the air–sea feedback limited the magnitude of the SST anomalies. More detailed analyses by Reynolds (1978), Frankignoul (1979), and Frankignoul and Reynolds (1983) indicated that away from coasts and regions of strong currents much of the midlatitude SST variability can be explained using stochastic climate theory. Recently, models driven by stochastic forcing have been used to examine atmospheric variability (Farrell and Ioannou 1993; Newman et al. 1996, manuscript submitted to *J. Atmos. Sci.*), the thermohaline circulation in the ocean (Mikolajewicz and Maier-Reimer 1990); Griffies and Tziperman 1995), and El Niño (Lau 1985; Penland and Sardeshmukh 1995).

Interactions between the surface and deeper ocean layers may also influence SST anomalies. Namias and Born (1970, 1974) noted a tendency for midlatitude SST anomalies to recur from one winter to the next without persisting through the intervening summer. They speculated that temperature anomalies that form at the surface and extend into the relatively deep ocean mixed layer in winter, could remain intact in the seasonal thermocline during the following summer. The anomalies would be insulated from surface processes by the reformed, shallow mixed layer and could then reappear at the surface when the mixed layer again deepened in the following fall/winter via entrainment. This "re-emergence mechanism" was examined in greater detail by Alexander and Deser (1995) using subsurface ocean temperature measurements collected at ocean weather stations (OWSs) and simulations with a mixed layer model. They concluded that the reemergence of SST anomalies from one winter to the next appeared to occur at several locations in the North Atlantic and North Pacific Oceans.

Many studies, including Elsberry and Garwood (1978), Miyakoda and Rosati (1984), Martin (1985), and Large et al. (1994) have used mixed layer ocean models driven by observed atmospheric conditions to examine midlatitude SSTs. In this study, we use atmospheric data collected at OWS P in the northeast Pacific (50°N, 145°W) to derive an extended time series of surface atmospheric variables with statistical characteristics similar to the original observations. The simulated atmospheric variables are then used in computing the surface boundary conditions for a variable depth mixed layer ocean model. The results from this model run are then compared to ocean data and used to investigate temperature variability in the upper ocean, the re-emergence mechanism, and the relative importance of competing terms in the mixed layer model's heat budget.

There are several benefits of using stochastic forcing instead of the actual atmospheric data as boundary conditions for the ocean model. This experiment design enables us to extend the work of Frankignoul and Hasselmann (1977) by including a variable depth ocean and stochastic surface forcing whose spectrum is not white. A second benefit is the ability to perform very long simulations, which allows for multiple occurrences of upper-ocean features, enhancing the signal to noise ratio in our model calculations. In a statistical sense the model's behavior is well sampled and thus error bars about the results from such a simulation are very small. The longest nearly continuous surface data records are only about 30 years long, and a model run of this duration may provide a sample that is not representative of the true model behavior.

A third benefit of using stochastic forcing is that it provides a better test of the model's fidelity. Using the actual surface atmospheric variables or even the observed surface energy fluxes as boundary conditions strongly constrains the ocean model to track observations, giving a false impression of the model's accuracy. For example, anomalous ocean heat advection could lead to SST anomalies, which then influence the overlying atmosphere, as the air and sea temperature tend to come in to equilibrium on interannual timescales. A one-dimensional ocean model driven by these atmospheric conditions may obtain realistic SSTs even though the model contains no ocean currents. Another example results from seasonal autocorrelations in the observed surface energy fluxes. If the fluxes are strongly correlated in spring and fall it would be difficult to isolate the role of entrainment in the re-emergence mechanism from upper-ocean temperature anomalies, which are primarily responding to surface forcing. Low-frequency variability of the atmospheric variables in the stochastic model occurs randomly as the decay time of anomalies are short (<1 month) and they evolve independently of the SSTs. Thus, the low-frequency variability of model SSTs is due to the dynamics of the model rather than a simple forced response. Surface fluxes are computed with SSTs from the mixed layer model to allow for damping caused by air–sea feedback, an important process in the real world.

Here a stochastic/physical model of the air–sea system is used to address questions concerning how surface energy fluxes and the entrainment of water into the mixed layer from below influence midlatitude SST

anomalies. Entrainment is very difficult to measure from observations and few studies have examined its impact on SSTs. Haney and Davies (1976) investigated the role of entrainment on the mean seasonal cycle, while Camp and Elsberry (1978) performed ~50 case studies to examine the relative effect of entrainment and the net surface energy flux on SSTs during storms. However, the net influence of entrainment on SST anomalies over the course of the seasonal cycle is not well known. If entrainment does affect SST anomalies, is it via changes in the entrainment rate, the temperature of the entrained water, and/or the mixed layer depth? What is the relative importance of wind stirring, surface buoyancy forcing, and the stability of the upper ocean on entrainment and the depth of the mixed layer? And to what extent does subsurface heat storage and the subsequent entrainment of these thermal anomalies into the mixed layer influence SST?

These questions are addressed using a 500-yr simulation of the statistical atmosphere/physical ocean model. The observations at P, the stochastic atmosphere and mixed layer ocean models, the surface flux parameterizations, and procedures for model verification are described in section 2. Simulations of the mean seasonal cycle and its variability are presented in section 3. In section 4, the temporal characteristics of the simulated ocean temperature and mixed layer depth anomalies are shown and compared with observations and stochastic theory. In this section we also explore the response of the model to atmospheric forcing associated with El Niño. The seasonal recurrence of SST anomalies and relationships between surface forcing, entrainment, and ocean variability, are examined in sections 5 and 6, respectively. The results are summarized and discussed in section 7.

2. Observations and modeling of conditions at OWS P

a. Data and analyses methods

Ocean weather stations were established in the North Atlantic and Pacific at the end of World War II to participate in search and rescue missions and to collect data. They are unique in oceanography in having long-term, nearly continuous records at the same location. OWS P, in the Gulf of Alaska, was chosen in this study because of its long record of high quality surface and subsurface data and because it is located far from strong currents, so that a one-dimensional model may be adequate for examining conditions there. Surface observations of air and dewpoint temperature, wind speed, sea level pressure, cloud fraction, etc., were taken almost continuously from 1950 to 1979 in 3-h intervals. Average daily atmospheric values, used to compute the stochastic variables, were calculated for days with six or more observations. Air–sea energy exchange is computed using the stochastic atmospheric values and SSTs provided by the mixed layer model. Results from the mixed layer model simulation are compared with subsurface data collected using mechanical bathythermographs (MBTs) at OWS P from 1953 to 1974. Ocean temperatures were routinely recorded at 5 m increments from the surface to a maximum depth of 135 m prior to 1957 and 270 m thereafter. Additional information about the surface and subsurface data and data processing can be found in Alexander and Deser (1995).

One method used to test the simulated ocean and atmosphere quantities is to compare their spectral characteristics with observations. SST and mixed layer depth spectra are calculated using monthly anomalies, estimated from the departure of the average of the individual observations within a given month from the long-term monthly mean. To compute daily spectra of atmospheric observations, we linearly interpolated across data gaps of one or, at most, two days and were left with eight nonoverlapping time series segments, each at least 2 years long. Segments of daily data smaller than this length were not used to calculate spectra. Spectra were obtained using Thomson's (1982, 1990) multitaper method (MTM), designed to minimize both the "leakage" inherent in discrete Fourier spectral analysis and the variance of the spectral estimate. Leakage occurs when the true frequency of a spectral peak lies somewhere between the frequencies at which a discrete Fourier transform is evaluated. Thomson's insight was that the reliability of the spectral estimates could be increased while minimizing leakage out of a frequency band by applying multiple tapers to the time series and averaging the results. The number of appropriate tapers involves a trade-off between leakage and variance; we used seven tapers, which results in fairly smooth spectra. A detailed description of the MTM method is given by Yiou et al. (1991) and several studies have applied MTM analyses to observed times series, including Slepian (1983) and Vautard et al. (1992).

b. The stochastic atmospheric model

Frankignoul and Hasselmann (1977) suggested that the atmospheric forcing of SST anomalies could be parameterized as white noise with constant variance. Here, we extend their model by including atmospheric variability whose variance is time dependent, and whose spectrum is not white. Our philosophy for developing the stochastic atmospheric model was to derive the simplest model that could reproduce most of the observed properties. The four atmospheric variables included in the model are the anomalous air temperature (T_{air}), dewpoint temperature (T_{dew}), shortwave radiation (q_{sw}), and wind speed (V). With the exception of T_{air} and T_{dew}, correlations between daily anomalies in these variables are small, with magnitudes of less than 0.2 (Table 1). Thus, anomalies in T_{air}, q_{sw}, and V are computed independently using different Markov

TABLE 1. Correlations between air temperature, dewpoint temperature, wind speed, and shortwave radiation at the surface using daily values.

	T_{air}	T_{dew}	V	q_{sw}
T_{air}	1.00			
T_{dew}	0.84	1.00		
V	−.03	0.02	1.00	
q_{sw}	−.06	−.18	−.07	1.00

models, while T_{dew}, which predominantly depends on the T_{air} anomaly, is calculated from a regression relationship. The four atmospheric anomaly models are described in the appendix. The stochastic anomalies are then added to the daily climatological values of the respective variable, thereby including the mean seasonal cycle. The diurnal cycle is not represented, but the atmosphere and ocean models are integrated using a 1-h time step in order to obtain reasonable statistics for the stochastic atmospheric variables.

Here, T'_{air} was modeled using a combination of two noninteracting linear Markov processes, where the two decay timescales are likely associated with different physical mechanisms. The faster Markov process represents the passage of storms. The slower system includes variability associated with ultralong waves (Hartmann 1974) and the associated passage of different air masses (Fissel et al. 1976). It also includes the effect of thermal feedback of SST anomalies on the local air temperature (Frankignoul 1985) so that some air–sea coupling is implicitly included in the model. The spectra of T'_{air} from the eight observed time series segments (dotted lines) along with the spectrum from the stochastic model (bold line) are shown in Fig. 1a. Both the observed and simulated spectra are red for periods less than ~200 days and have nearly constant variability at longer periods. The flattening of the simulated spectra at lower frequencies results from linear damping, as described in the appendix. The simulated spectrum falls within the spread among the observed spectra at nearly all periods. However, the model tends to have less variability compared with the mean of the eight observed spectra at periods less than about 20 days but more variability at periods longer than 50 days. Before including the fast Markov process, the T'_{air} model overestimated the increase in variability with period for periods less than ~150 days (cf. Alexander and Penland 1995).

A scatterplot between T'_{dew} and T'_{air} is shown in Fig. 1b. Given that the correlation between the two is nearly 0.85, we were able to model T'_{dew} from a regression on T'_{air}, with a random component added to account for the independent variability.

The observed daily q'_{sw} values are derived from the formula developed by Reed (1977), which depends on the solar radiation at the top of the atmosphere, the cloud fraction, and the surface albedo (obtained from Payne 1972). This variable is modeled using a single linear Markov process, but one whose parameters changes with the time of year. In contrast to T'_{air}, the spectra of observed and modeled q'_{sw}, shown in Fig. 1c, are nearly white at periods longer than about 10 days.

The prognostic model for the wind speed anomalies consists of a linear system driven by both multiplicative and additive white noise forcing. Including multiplicative noise, where the variable, V', is multiplied by a random component, enhanced the variability at less then 10 days enabling an especially good fit to the data on these timescales (Fig. 1d). The model and observed spectra are red at periods less than 20 days, nearly white for periods between 20 and 150 days, but then show a slight increase in variability at 200 days. Hartmann (1974) and Fissel et al. (1976) have found enhanced variability on synoptic timescales, ~5 days, in some atmospheric quantities over the oceans. While maxima at these timescales are not readily apparent from the observed MTM spectra shown in Fig. 1, when the observed wind speed spectra are subjected to the smoothing procedure described by Fissel et al. (1976), the broad synoptic peak between 2 and 10 days, which they detected at OWS P, is also found in our data (not shown).

c. *Mixed layer ocean model*

The near-surface layer of much of the world's oceans is vertically well mixed with nearly uniform temperature and salinity. A one-dimensional ocean model developed by Gaspar (1988), which has been formulated with climate simulations in mind, is used to examine the influence of surface forcing and entrainment on the temperature and depth of the mixed layer. The temperature tendency of the mixed layer is controlled by the net surface energy flux, penetrating solar radiation, entrainment and diffusion:

$$\frac{\partial T_m}{\partial t} = \frac{q_{net} - q_{swh}}{\rho c h} - \frac{W_e \Delta T}{h} + \frac{\nu_h}{h}\frac{\partial T}{\partial z}\bigg|_{z=h}, \quad (1)$$

where T_m is the mixed layer temperature, $\Delta T = T_m - T_b$, T_b being the temperature just below the mixed layer, W_e is the entrainment rate, ρ the density of seawater, h the mixed layer depth, q_{net} the net surface energy flux into the ocean, q_{swh} the penetrating solar radiation at h, ν_h the molecular diffusion coefficient for heat, and z the vertical coordinate (positive downward). We chose to specify salinity in the model according to climatology, since long time series of precipitation data over the oceans, which strongly influences salinity, are unavailable. Since salinity influences the density profile and, thus, h, its impact on variability in the surface layer should be examined in the future.

The mixed layer depth increases via entrainment, which depends on the surface buoyancy forcing, wind stress, and penetrating solar radiation. The entrainment

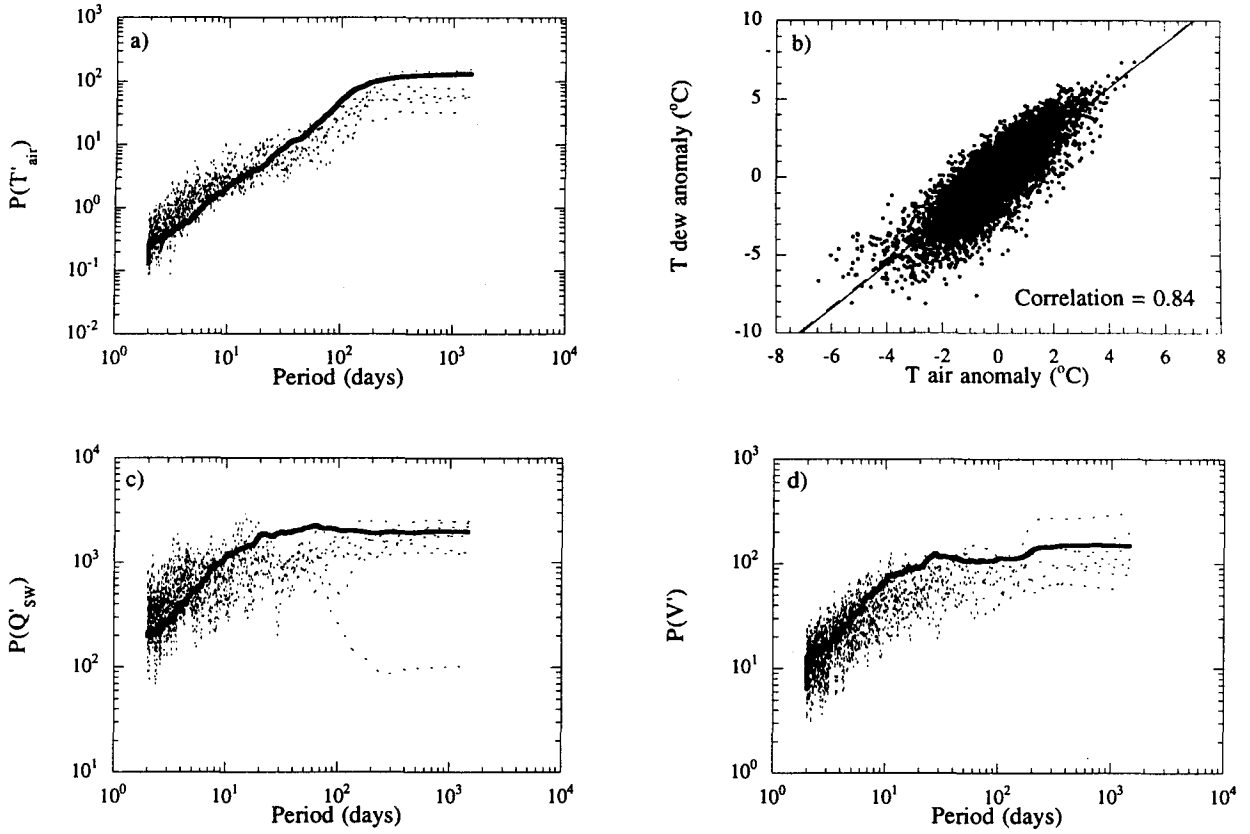

FIG. 1. Observed (dashed lines) and simulated (bold line) spectra for (a) T_{air}, (c) q_{sw}, and (d) V, computed using the multitaper method. The observed spectra are calculated using daily data from eight independent 2-yr periods at OWS P, the model spectrum is from an average of 60 2-yr periods. (b) Scatterplot of the observed daily values of T_{dew} vs T_{air} (°C).

equation [see Eq. (50) in Gaspar 1988] has several adjustable parameters; we have used Gaspar's estimates of these time-independent parameters in all of our simulations. When deepening, h is computed as a prognostic variable; when shoaling, the mixed layer reforms closer to the surface, entrainment is set to zero, and h is computed as a diagnostic quantity by assuming a balance between wind stirring and surface buoyancy forcing. When the mixed layer shoals, the temperature profile is adjusted according to Adamec et al. (1981), in order to conserve both heat and potential energy.

The region beneath the mixed layer is represented by a multilayer system, where heat is redistributed through convective overturning, vertical diffusion, and penetrating solar radiation. The vertical diffusion is calculated using a constant coefficient of 2×10^{-5} m s^{-2}, estimated from analyses of subsurface data in the Pacific by White and Bernstein (1981). The absorption of solar radiation is parameterized following Paulson and Simpson (1977). The model contains 30 unequally spaced layers between the surface and 1000 m, 15 of the layers are within the first 100 m in order to adequately resolve the summer thermocline. The temperature of layers that are entirely above h are set to T_m, while T_b is obtained directly from the layer in which h resides. The mixed layer model is described in more detail by Battisti et al. (1995), while Alexander and Deser (1995) present results from model simulations where the observed atmospheric conditions at P and at OWS C (in the north Atlantic) are used as boundary conditions.

d. *Surface flux parameterization*

The exchange of heat and momentum across the ocean surface are computed using standard bulk aerodynamic formulas (e.g., Gill 1982; Kraus and Businger 1994). The net surface energy flux, q_{net}, defined here to be positive for fluxes which heat the ocean, is composed of the shortwave radiation, q_{sw}; net longwave radiation, q_{lw}; and the sensible and latent heat fluxes, q_{sh} and q_{lh}, respectively. The method used to obtain q_{sw} is described in section 2b; q_{lw} is computed using the formula of Isemer and Hasse (1987) and depends on the SST, T_{air}, and the daily average cloud fraction. The bulk transfer coefficients used in computing q_{sh} and q_{lh} and the wind stress, τ, are calculated using the formulas of Large and Pond (1982) and Large et al. (1994),

which depend on wind speed and the air–sea temperature difference. The surface energy fluxes are computed using T_m from the model, which is assumed to be equal to the SST.

Errors in the atmospheric forcing, including the parameterizations used to compute the surface fluxes, deficiencies in the mixed layer model, and the absence of horizontal processes in the ocean model, particularly heat advection, can all cause the simulated ocean temperatures to drift from observations. As in previous modeling studies (e.g., Sausen et al. 1988; Manabe and Stouffer 1988; and Battisti et al. 1995) the surface heat fluxes have been adjusted in order to obtain an accurate representation of the true mean ocean state. Following Alexander and Deser (1995), a constant 16 W m^{-2} is subtracted from the surface fluxes at each time step during the simulation, allowing for a reasonable simulation of the annual mean and seasonal cycle of SST.

e. Model verification

The model's fidelity is assessed by computing the pattern correlations between corresponding observed and simulated fields whose axes are calendar month and depth. The pattern correlation (PC) is given by

$$\mathrm{PC} \equiv \frac{\sum_{n=1}^{\text{mons}} \sum_{l=1}^{\text{levs}} (x_o - \hat{x}_o)(x_s - \hat{x}_s)}{\left[\sum_{n=1}^{\text{mons}} \sum_{l=1}^{\text{levs}} (x_o - \hat{x}_o)^2 \sum_{n=1}^{\text{mons}} \sum_{l=1}^{\text{levs}} (x_s - \hat{x}_s)^2\right]^{1/2}}, \quad (2)$$

where x is the value at a given month (n) and level (l), $\hat{x}$ is the field mean, and subscripts s and o indicate simulated and observed, respectively. While the statistical significance of the PC values can be tested using the t statistic (Snedecor and Cochran 1980), the true number of degrees of freedom is difficult to determine because of the interdependence of the data in both time and space. We estimate the number of degrees of freedom using the "N rule" described by Preisendorfer (1988, pp. 199–204). This method uses empirical orthogonal functions (EOFs) to find the number of eigenvalues that exceed a background noise level estimated from Monte Carlo simulations. This procedure, which gives a conservative estimate of the number of meaningful EOFs, indicates that the observed and simulated fields have 4 and 8 significant EOFs, respectively. Using a one-sided t test with 10 degrees of freedom, the sum of the significant EOFs in each system minus two, PC values of 0.50 (0.66) are significant at the 95% (99%) confidence level.

3. The seasonal cycle of the upper ocean

As a first step, we performed a 500-yr simulation in which the mixed layer model was driven only by the daily mean seasonal cycle of the surface fluxes (no stochastic forcing). The resulting simulated seasonal cycle of ocean temperature and mixed layer depth are compared with observations in Fig. 2. Following Levitus (1982), the observed h is defined as the level at which the temperature is more than 0.5°C less than the SST. In both the model and observations, the mixed layer extends to a maximum depth of ~150 m in March, then shoals rapidly in spring, reaching a minimum depth of ~25 m in July. The maximum SST, which exceeds 12°C, tends to occur 1 to 2 months after the minimum h is reached. The lag between the maximum SST and the temperature at a given level increases as the depth increases. A seasonal thermocline, where the temperature decreases rapidly with depth, forms in summer between the base of the mixed layer and 75–100 m. The model temperatures closely resemble observations as indicated by a PC value of 0.98 both before and after the annual mean is removed at each level; recall, however, that a small constant surface cooling was applied at each model time step. Model deficiencies include ocean temperatures that tend to be roughly 0.5°C too warm in winter and throughout the year below 100 m, and an underestimation of the amplitude of the seasonal cycle especially beneath the mixed layer.

The 500-yr simulation was then repeated with the stochastic atmospheric anomalies included. (Hereafter, discussion of the model results will primarily refer to this simulation.) The inclusion of stochastic forcing slightly improved the mean seasonal cycle of temperature (not shown); for example, the root-mean-square difference between the observed and simulated mean SST for the 12 calendar months is 0.26°C in the run with stochastic forcing and 0.36°C without it. However, the stochastic forcing results in a degradation of the simulated h (Fig. 3a); now, it is too shallow throughout the year, especially in spring as a result of the model shoaling 1–2 months too early.

Several factors may explain this discrepancy between the observed and the stochastically driven simulation of h: (i) Gaspar (1988) notes that most mixed layer models, including his, tend to shallow too rapidly under stable conditions. In the simulation with the mean seasonal cycle forcing, relatively strong winds and negative surface buoyancy forcing (upward net heat flux) maintain a deep h through late winter. In contrast, including stochastic forcing results in days with low wind and surface heat gain causing a reformation of h much closer to the surface. Once shallow, the model tends to resist mixing down to the previous depth. This also occurs in model simulations where the surface fluxes are computed from the actual daily data (not shown). (ii) The observed h has a diurnal cycle with an amplitude of ~10 m during the winter months (not shown), while the model does not contain a diurnal cycle. Diurnal variability results from the surface buoyancy forcing, which creates shallow but weak mixed layers during the day that are overturned by oceanic convection at night (Woods and Barkmann 1986). If the diurnal fluctuations in h are asymmetric about the

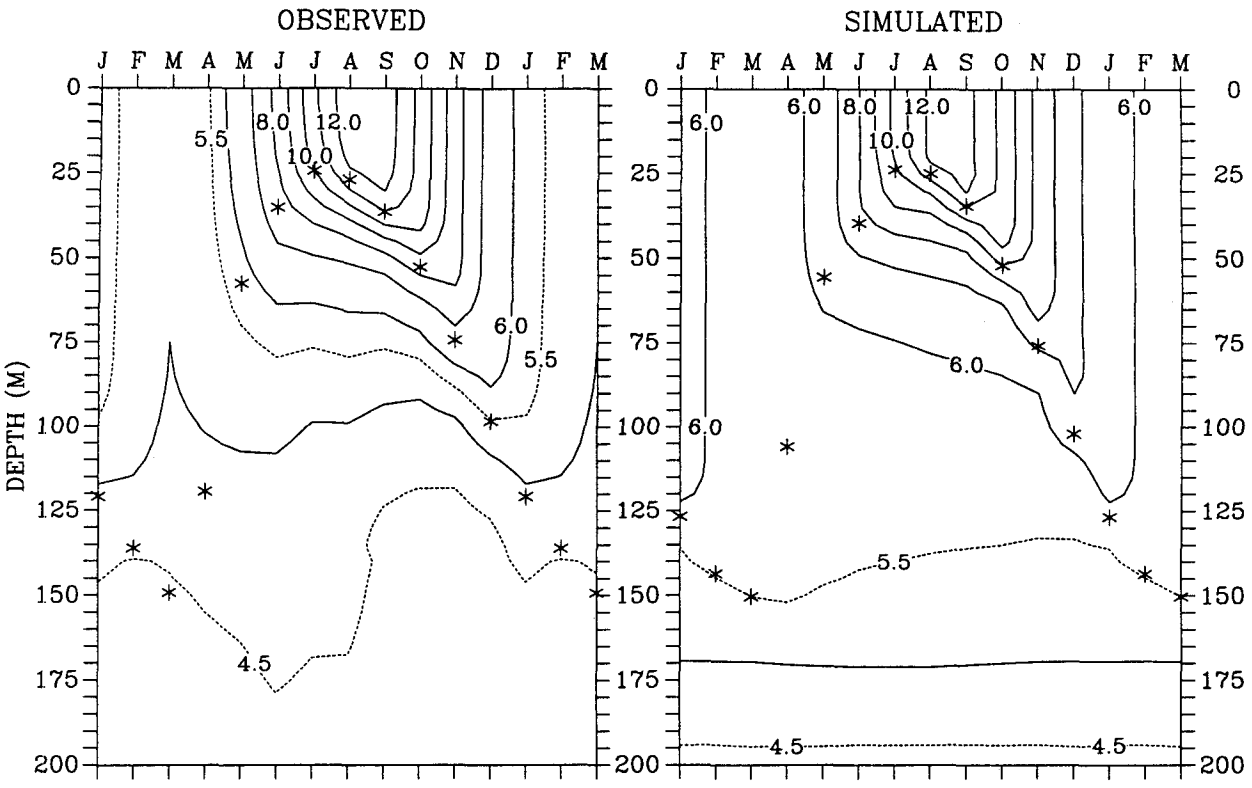

FIG. 2. Monthly mean observed and simulated temperature (°C) in the upper 200 m. Also shown is h, the mixed layer depth (*); the observed h is determined by finding the depth at which SST $- T_{depth} > 0.5$°C, while the simulated h is obtained directly from the model when its driven by the mean atmospheric seasonal cycle. Note that the first 3 months of the year are repeated in order to clearly display the seasonal cycle.

daily mean, they could influence the monthly average mixed layer depth. (iii) Compared with observations, the stochastic model has fewer occurrences of very strong surface heat loss ($q_{net} < -300$ W m^{-2}). Camp and Elsberry (1978), Elsberry and Garwood (1978), and Price et al. (1978) have shown that h increases rapidly during storms, when the buoyancy and mechanical forcing are large. (iv) Defining h where the temperature is 0.5°C colder than the surface, will tend to miss transient thermoclines that form in spring and is more representative of the lower extent of the seasonal thermocline (Gaspar 1988). Selecting a temperature threshold of 0.1°C, following Martin (1985) and Yan and Okubo (1992), results in smaller observed h estimates, although they are still deeper than the simulated h values by ~10–20 m in spring. (v) Salinity influences the density profile and hence the base of the mixed layer; at OWS P there tends to be a mean pycnocline at ~150 m. The mean salinity profile is included in the ocean model acting to constrain h, but salinity was not included in calculating the observed mixed layer depth as it was measured infrequently.

The standard deviation of monthly averaged h from the model and observations are shown in Fig. 3b. The maximum variability tends to occur when h shoals from its maximum mean depth in late winter/early spring. At this time of year the base of the mixed layer can reform more than 75 m closer to the surface and the timing of this shoaling can lead to large monthly variability in h. Thus, like the maximum mean mixed layer depth, the variability in h is smaller and occurs sooner in the model compared with observations. The largest h variability occurs in March (April) with a maximum standard deviation of 30 m (35 m) in the model (data).

In contrast to the mixed layer depth, the maximum variability in ocean temperatures occur in late summer/early fall in both the model and observations (Fig. 4). The maximum observed standard deviation of SST exceeds 0.8°C in August, October, and November, while the model exceeds 0.8°C in September.[2] During early fall the mixed layer is shallow (Fig. 3a) and both surface fluxes and entrainment can generate large changes in SST (see section 6). In both the model and data a region of enhanced subsurface variability extends from

[2] The SD of SST obtained from 30 years of surface observations is generally about 0.2°C larger than obtained from the MBT data used in Fig. 4, with values ranging from ~0.6°C from January–April and ~1.0°C from August–October.

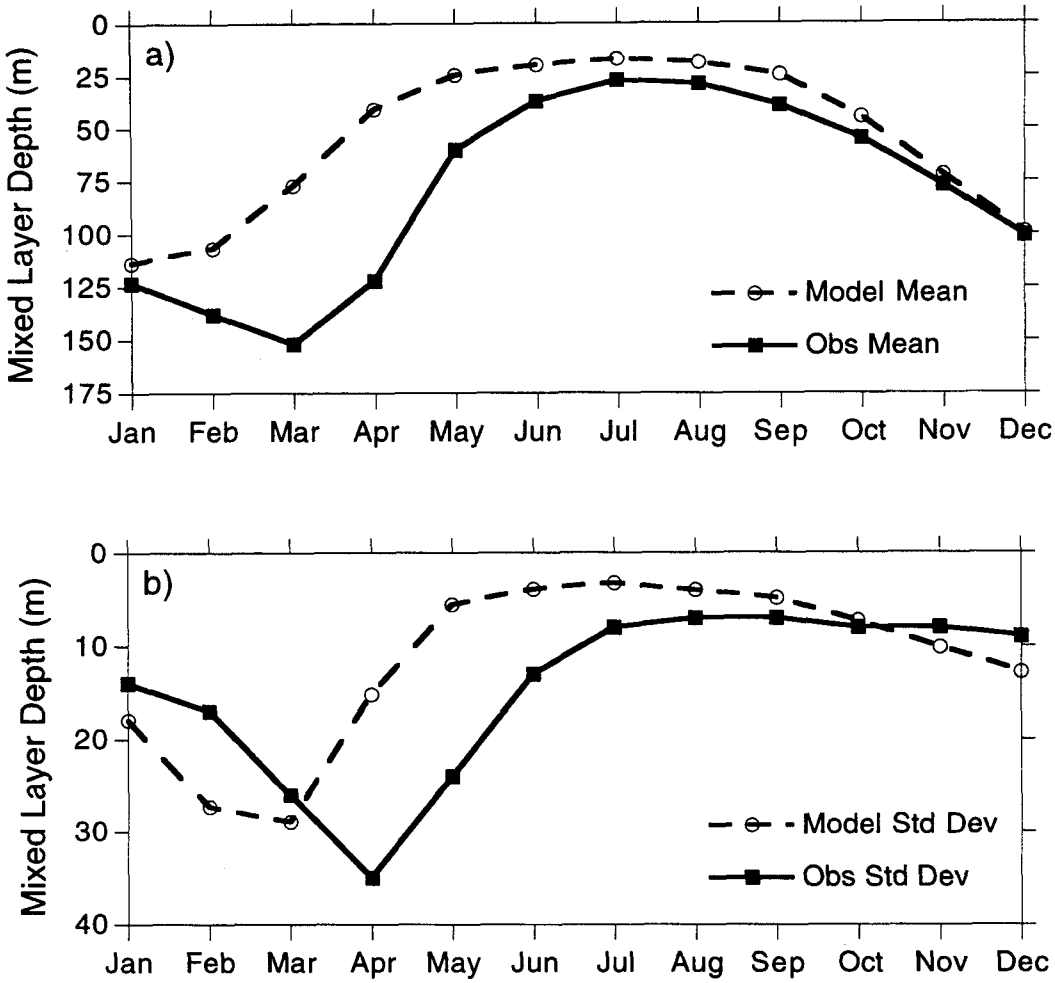

FIG. 3. Observed (solid line) and simulated (dashed line) (a) mean and (b) standard deviation of the monthly mixed layer depth (m). Here the model includes stochastic atmospheric forcing.

roughly 30 m in July to 75 m in November, and exceeds 0.9°C near 45 m during September. This axis coincides with the location of the mean h; displacements from the mean during summer and fall can result in large temperature anomalies as there are strong vertical gradients in the seasonal thermocline (Fig. 2). Although the model tends to underestimate the standard deviation range over the course of the seasonal cycle, it reproduces most features of the observed temperature variability, resulting in a significant PC value of 0.74.

4. Timescales of ocean variability

Numerous studies have tested mixed layer models by examining their ability to reproduce the mean seasonal cycle or by correlating simulated and observed SST anomalies. Gill (1979) states that it would be useful to test upper-ocean models by comparing simulated with observed spectra of SST time series. The spectra of monthly SST anomalies from the 500-yr stochastic run lie within the 95% confidence intervals of the MTM spectral estimates for the observations at nearly all frequencies (Fig. 5). However, the model tends to underestimate the variability at most frequencies, with values that are ~40% less than observed at periods of 20–50 months and 20% less for periods greater than a 100 months. Several processes missing from the model could account for this underestimate, including covariability between the stochastic atmospheric variables. While the correlations among T'_{air}, V', and q'_{sw} are negligible on daily timescales (Table 1), the covariability between variables increases at certain periods. For example, the correlation between monthly anomalies of V and T_{air} is −0.25, indicating that stronger winds are associated with colder air temperatures, which would enhance surface heat fluxes and the generation of SST anomalies. Tabata (1965) and Large et al. (1986) found evidence for subsurface heat convergence in the

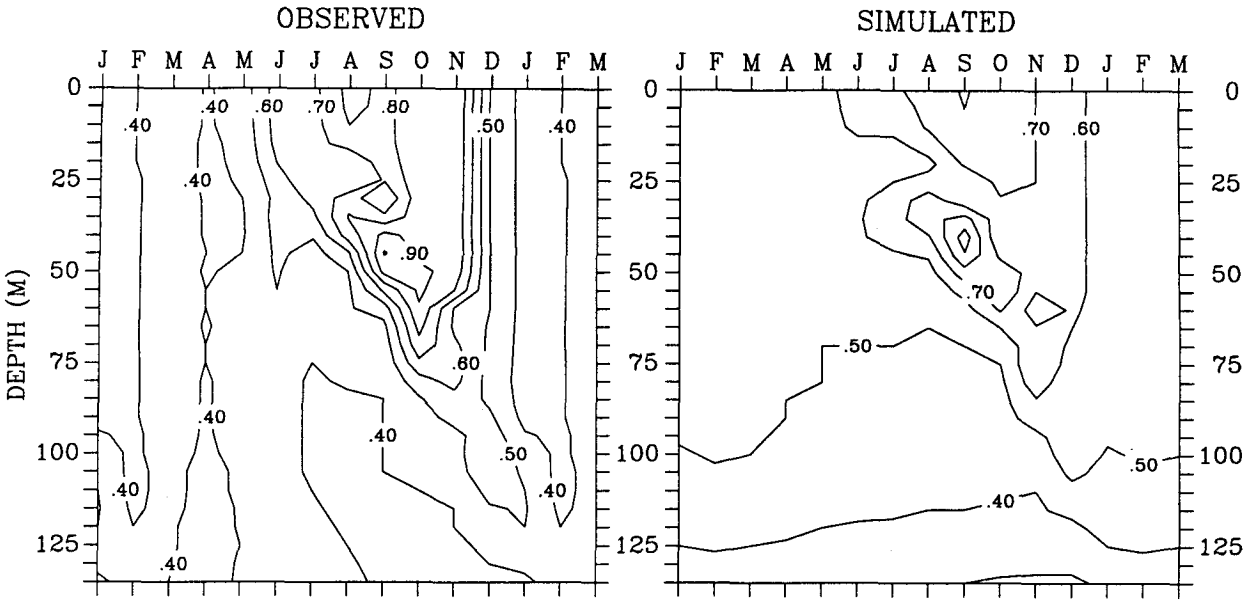

FIG. 4. Observed and simulated standard deviation of the monthly temperature anomalies (°C).

northeast Pacific during fall; fluctuations in the heat advection, not included in the model, could influence SST variability especially at longer periods.

The model also omits fluctuations in the strength and position of the Aleutian low associated with El Niño/Southern Oscillation (ENSO) in the tropical Pacific (Bjerknes 1969; Blackmon et al. 1983; Emery and Hamilton 1985), which have been shown to cause SST anomalies to form in the North Pacific (Alexander 1990, 1992; Lau and Nath 1996). To test the possible connection between ENSO and SST variability at OWS P, we performed an additional model experiment as follows. First, a long synthetic time series of SLP anomalies at Darwin, Australia, which is representative of the state of ENSO, is constructed using an autoregressive model developed by Trenberth (1996). Then, correlation and regression values for each calendar month are calculated between the observed 3-month running mean of SLP′ at Darwin and monthly anomalies of atmospheric variables in the vicinity of OWS P obtained from the Comprehensive Ocean–Atmosphere Data Set (COADS). Only the air and dewpoint temperatures near P are found to be significantly correlated with Darwin SLP between 1949 and 1992 when good data are available from COADS. Next, the observed regression values of T'_{air} on Darwin SLP are multiplied by the simulated Darwin pressure anomalies to generate a 500-yr time series of monthly air temperature anomalies at P "associated with ENSO." Finally, these T_{air} anomalies are interpolated to daily values using a cubic spline and then added to the stochastic atmospheric model; the resulting change in humidity is included via Eq. (A4). We note that the ENSO signal can be added directly to the atmospheric forcing as it operates at a much longer timescale (>20 months) and is nearly independent from the stochastic processes whose decay times are all less than a month.

Spectra of the monthly SST′ from observations, the original model, and the mixed layer model run driven by the stochastic plus ENSO forcing are shown in Fig. 5b. Including the ENSO signal enhances the variability in the mixed layer model and results in a better fit to the observed spectra for periods greater than ~2 years. The difference between the two model runs indicates that the SST anomalies at P associated with teleconnections to ENSO result in a red spectra up to periods of ~100 months without large peaks in the spectra, consistent with the recent findings of Lau and Nath (1996). We also performed a similar experiment in which the ENSO signal was provided by a linear inverse model of SSTs in the tropical Pacific (Penland 1996); the SST′ spectrum at P from this model (not shown) were within 6% of those forced by Darwin SLP model.

Linear stochastic climate theory (Hasselmann 1976) suggests that SST anomalies can be represented by a first-order Markov process with the ocean response in the frequency domain given by

$$G(\omega) = \frac{F}{(\omega^2 + \lambda^2)}, \qquad (3)$$

where F is the variance of the white noise forcing, ω the angular frequency, and λ the linear damping factor. In such a system, which represents a fixed depth ocean without currents driven by white noise, the SST anomaly variance at high frequencies increases with the square of the period, indicated by a line with a slope

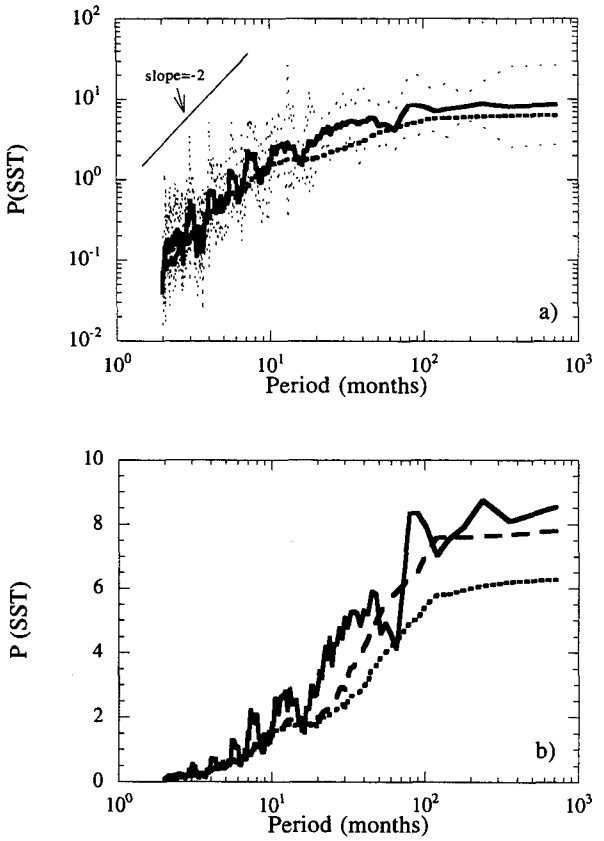

FIG. 5. Observed (thick solid line) and simulated (thick short dashed line) spectra of monthly SST′ calculated with the multitaper method using (a) log–log, (b) log–linear (in y) axes. The simulated spectra is from an average of 16 30-yr periods. In (a) the thin dashed lines show the 95% confidence interval about the observed spectra. The line in the upper left corner has a slope of 2, representing the increase in variance with the square of the period as predicted by Hasselmann's stochastic theory. In (b) the long dashed line depicts a model simulation in which atmospheric forcing associated with ENSO is included.

of 2 at high frequencies ($\omega \gg \lambda$) on a log–log plot (Fig. 5a). The slope obtained by a linear fit to the SST′ spectrum for periods less than a year is 1.90 in the mixed layer model, closer to the observed value of 1.75 than the Markov model. The subtheoretical observed and simulated slopes may result from inclusion of more than one timescale in the atmospheric forcing, and nonlinearities in both the surface flux formulas and within the ocean model. On longer timescales, negative feedbacks associated with air–sea interaction and entrainment suppress the variability, causing the spectra to become white at periods greater than ~150 months. In Hasselmann's stochastic climate theory this occurs when $\omega \ll \lambda$, as indicated by Eq. (3).

Autocorrelations of SST′ indicate the rate at which anomalies decay and provide a means of estimating λ. The log of the observed and simulated SST anomaly correlations out to lags of 15 months are shown in Fig. 6. SST anomalies decay slightly faster in the model than in observations at lags of less than 7 months, while the reverse is true at longer lags. Linear stochastic theory indicates that the points in Fig. 6 should lie along a straight line with slope $-\lambda$. Here λ is estimated by minimizing the mean square difference between the monthly SST autocorrelation values $C(\tau)$ and the correlation function appropriate to Hasselmann's stochastic model, which has the form $\exp(-\lambda\tau)$. The damping timescale, λ^{-1}, calculated from the data (model) is 3.1 (2.9) months when lags up to 15 months are included; λ^{-1} decreases slightly when fewer lags are included. Stochastic theory gives an excellent fit to the model and data for lags of 5 months or less, but underestimates the correlation at greater lags. One reason for the deviation from a constant SST decay rate is that the mixed layer depth and, thus, the thermal inertia vary with the seasons. In addition, the slight enhancement of SST′ correlations from the model at 9–11 months lag (Fig. 6), first noted in the observed SSTs over the North Pacific by Namias and Born (1970, 1974), is related to the re-emergence mechanism as discussed in the following section. This feature is less pronounced in the observed SSTs at P, but the decay rate still decreases more slowly than the Markov model estimate.

The spectra of the observed and simulated mixed layer depths for the non-ENSO case are shown in Fig. 7. The model tends to underestimate the variability at nearly all frequencies and drops below the lower error limit of the observations for periods greater than ~80 months. Including the effect of ENSO forcing does enhance the model's mixed layer depth spectrum at low frequencies by 20%–30%. However, the model spectrum still lies below the observed confidence intervals

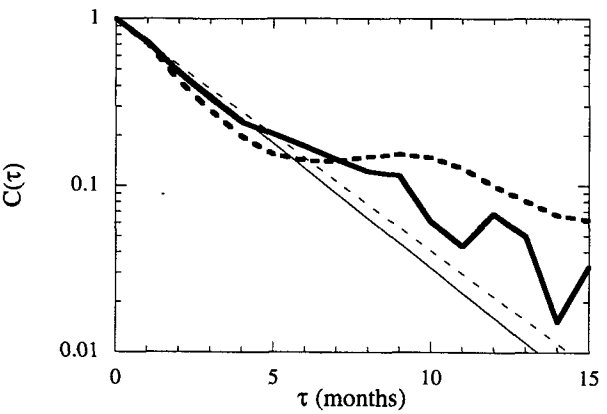

FIG. 6. Log plot of the observed (thick solid line) and simulated (thick dashed line) autocorrelation [$C(\tau)$] of monthly SST′, where τ is the lag in months. Thin solid (dashed) line, which represents a first-order Markov process, is obtained by minimizing the mean square difference between the observed (simulated) monthly SST autocorrelation values and the function $\exp(-\lambda\tau)$. The decay constant λ^{-1}, estimated from the data (model), is 3.1 (2.9) months when lags up to 15 months are included.

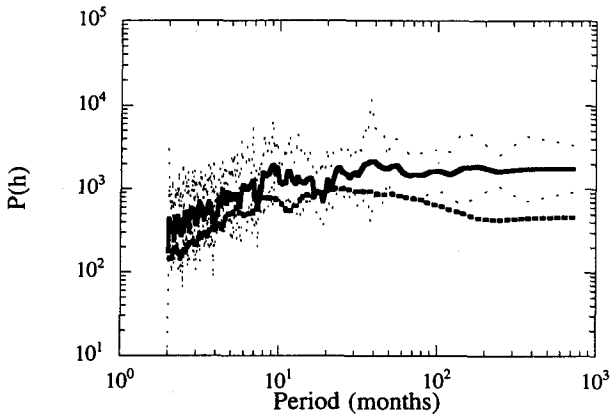

FIG. 7. Observed (thick solid line) and simulated (thick dashed line) spectra of monthly mixed layer depth anomalies, computed as in Fig. 5. Thin dashed lines represent the 95% confidence interval about the observed spectra.

for periods greater than 100 months. The reasons for this deficiency are unclear but not completely unexpected given the difficulty in both simulating h and estimating it from observations, as discussed in section 3.

5. The recurrence of SST anomalies

Alexander and Deser (1995) found evidence that ocean temperature anomalies created over the deep mixed layer in winter could be maintained within the summer seasonal thermocline and then reappear at the surface when they are entrained into the mixed layer in the subsequent fall/winter. They examined this reemergence mechanism by correlating ocean temperature anomalies in a base region within the summer thermocline with temperatures at depth during the previous and following 8 months. A similar analysis is performed here using observations and the stochastic model run with 45–55 m in August serving as the base region (Fig. 8). In both the data and the model a clear connection between surface temperature anomalies in spring with those in the summer seasonal thermocline is indicated by the 0.8 contour, while SSTs in summer are uncorrelated with concurrent temperatures in the base region. The correlations between the base region and the surface layers increase from summer to winter reaching a maximum in January of 0.46 (0.35) in the observations (model). While the model pattern is slightly more diffuse than the observed, the overall correspondence between the two is quite good as indicated by a PC value of 0.84, which is significant at the 99% level.

The magnitude of the anomalies and the difference between warm and cold cases is examined using composites of the temperature anomalies. Warm and cold composites, shown in Fig. 9, are constructed based on when the temperature anomaly in the base region exceeds plus or minus one standard deviation. The observed composites are based on an average of four to six values at each month/depth, while 78 values were used for the simulated composites. The PC between the observed and simulated warm and cold composites are

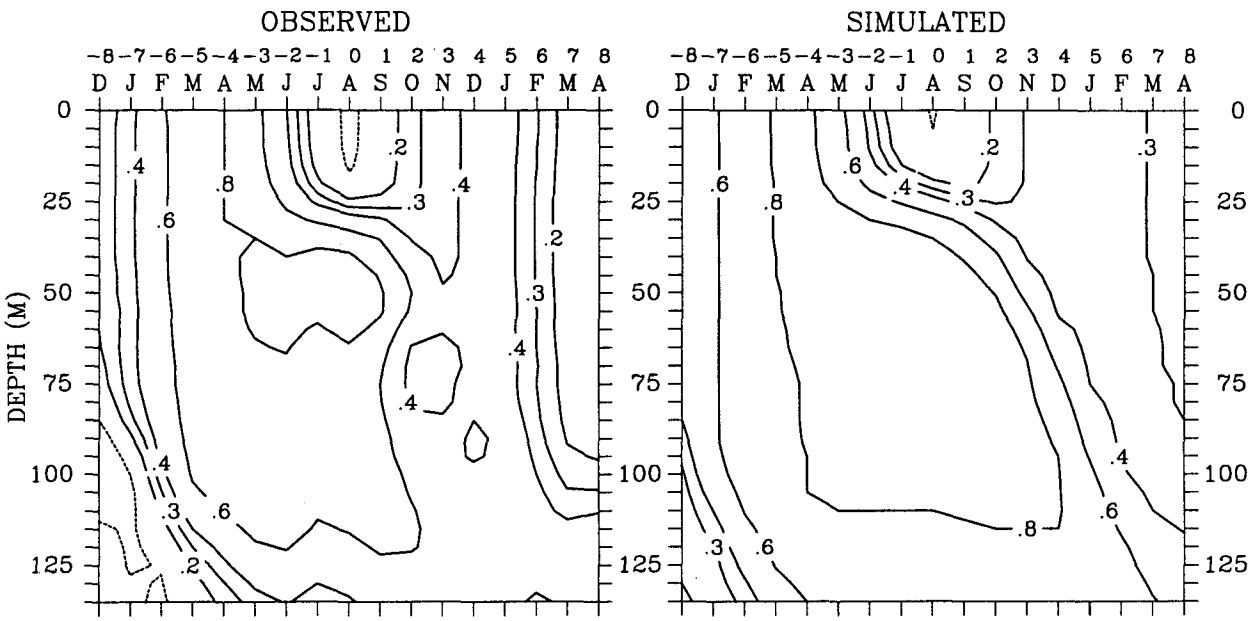

FIG. 8. Observed and simulated lead/lag correlations between the temperature anomaly in the base region 45–55 m in August and temperature anomalies in 5-m increments for the previous and following 8 months. The contour interval is 0.2 with the addition of the 0.3 contour. The data have been smoothed using 1-2-1 filter in time.

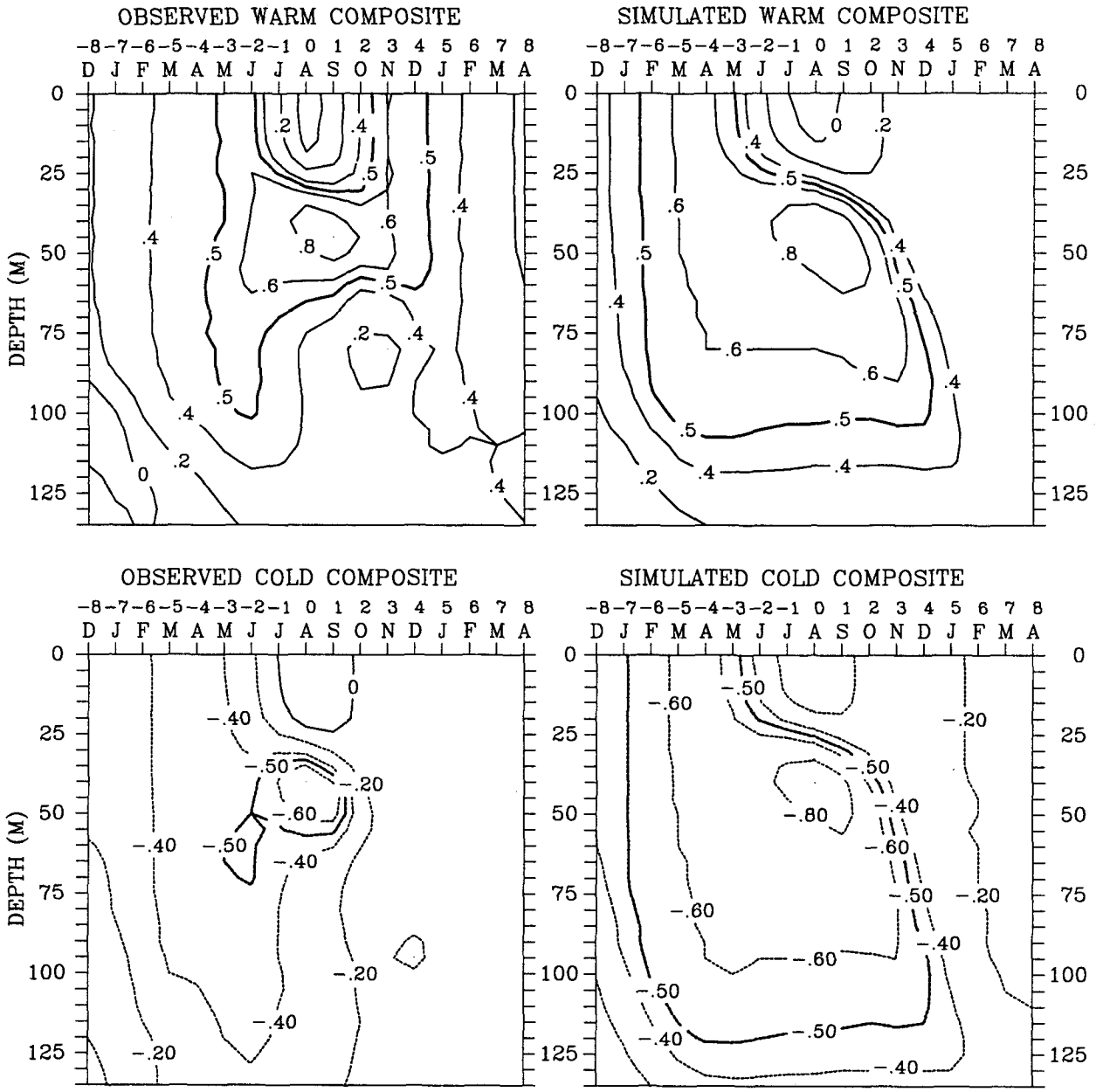

FIG. 9. Observed and simulated warm (cold) temperature composites to 135 m of monthly temperatures based on when the temperature between 45 and 55 m during August, is greater (less) than one standard deviation, ~0.4°C. Approximately 5 (80) values are included at each point in the observed (simulated) composite. The data have been smoothed using 1–2–1 filter in time. The contour interval is 0.2°C and the 0.5°C contour is also shown in bold.

0.64 and 0.81, significant at the 95% and 99% level, respectively. Like the lead–lag analyses, the composites support the re-emergence mechanism, with anomalies of one sign in the surface layers in spring moving to the seasonal thermocline in summer and returning to the surface layers in fall. However, the return branch is weak with the exception of the observed warm composite. We note that due to the small data sample the details of the observed composites were sensitive to the choice of the base region; the lack of observations likely contributes to some of the model data differences.

In the observed warm composite, the 0.5°C contour extends from the surface in late spring down to between 30 and 60 m in summer and then returns to the surface in the following November. The model reproduces the first part of this pattern, the 0.5 contour extends from the surface in spring downward into the summer ther-

mocline. However, in the simulated warm composite positive anomalies cover a much thicker layer in summer and only a weak warming occurs at the surface in the subsequent winter, when the SST′ is between 0.2° and 0.3°C from November through March. The difference in the observed and simulated temperature profile in summer may influence the re-emergence of the temperature anomalies in the following fall. In the observed warm composite, entrainment of the heat concentrated in a thin layer leads to strong warming in November, which then dissipates by March; while in the model, the entrainment of heat spread over a thicker layer in summer, subsequently heats the surface layer less intensely but over a longer period of time.

While the warm and cold composites generally resemble each other there are differences between the two. In both the observed and simulated cold composite the T'_m develops earlier in the year and extends downward through a deeper mixed layer relative to the warm composite. In addition, the anomalous cold water extends over a ~25-m thicker layer in the summer. The cold anomalies penetrate deeper than warm anomalies as they are more dense relative to the ambient water.

6. The influence of surface forcing and entrainment on SST and h

Entrainment is very difficult to measure yet may play an important role in heat budget of the surface layer in the ocean. Here, we investigate the relative roles of entrainment and the net surface energy flux on the development of SST anomalies over the course of the seasonal cycle using the 500-yr mixed layer model simulation. Entrainment can influence SSTs directly via the heat flux through the base of the mixed layer and indirectly by controlling the mixed layer depth, the thickness of the layer over which the fluxes act. The magnitude of both of these processes, as well as those which control anomalies in mixed layer depth, are examined in detail below.

Splitting the variables into daily mean ($\bar{\ }$) and departures from the mean ($'$), and given that $q_{\text{net}} \gg q_{\text{swh}}$ and that the diffusion of heat at h is small, the mixed layer temperature tendency equation (Eq. 1) can be approximated by

$$\frac{\partial(\bar{T}_m + T'_m)}{\partial t} = \frac{\bar{q}_{\text{net}} + q'_{\text{net}}}{\rho c(\bar{h} + h')} - \frac{(\bar{W}_e + W'_e)(\overline{\Delta T} + \Delta T')}{\bar{h} + h'}. \quad (4)$$

Using Taylor's expansion for $(\bar{h} + h')^{-1}$ assuming $h'/\bar{h} < 1$,[3]

$$\frac{1}{(h' + \bar{h})} = \frac{1}{1 + h'/\bar{h}} \approx 1 - \frac{h'}{\bar{h}} + \text{higher-order terms},$$

the anomalous mixed layer temperature tendency can then be approximated by

$$\frac{\partial T'_m}{\partial t} \approx \underbrace{\frac{q'_{\text{net}}}{\rho c\bar{h}}}_{\text{I}} - \underbrace{\frac{\bar{q}_{\text{net}}h'}{\rho c\bar{h}^2}}_{\text{II}} - \underbrace{\left(\frac{q'_{\text{net}}h'}{\rho c\bar{h}^2} - \frac{\overline{q'_{\text{net}}h'}}{\rho c\bar{h}^2}\right)}_{\text{III}} - \underbrace{\frac{W'_e\overline{\Delta T}}{\bar{h}}}_{\text{IV}} - \underbrace{\frac{\bar{W}_e\Delta T'}{\bar{h}}}_{\text{V}} - \underbrace{\left(\frac{W'_e\Delta T'}{\bar{h}} - \frac{\overline{W'_e\Delta T'}}{\bar{h}}\right)}_{\text{VI}}$$

$$+ \underbrace{\left[\frac{\bar{W}_e\overline{\Delta T}h'}{\bar{h}^2} + \left(\frac{W'_e h'\overline{\Delta T} - \overline{W'_e h'}\Delta\bar{T}}{\bar{h}^2}\right) + \left(\frac{\bar{W}_e\Delta T'h' - \bar{W}_e\overline{\Delta T'h'}}{\bar{h}^2}\right) + \left(\frac{W'_e\Delta T'h' - \overline{W'_e\Delta T'h'}}{\bar{h}^2}\right)\right]}_{\text{VII}}, \quad (5)$$

where terms I–III and IV–VII are derived from $(q_{\text{net}}/\rho ch)'$ and $[-(W_e\Delta T/h)]'$.

To examine how the terms in (5) influence the development of SST anomalies over the seasonal cycle, each term is calculated using the daily mean output from the non-ENSO model simulation and then averaged over a month. A composite of each term is constructed for the 12 calendar months based on when the monthly value of $\partial T'_m/\partial t$ exceeds one standard deviation, which varied from ~0.4°C mo^{-1} in February to 1.4°C mo^{-1} in August; approximately 80 monthly values went into each composite. A composite of the most rapidly cooling SST anomalies was also computed but not presented as the results are broadly similar but with the signs reversed, suggesting that the dynamics of the model are only weakly nonlinear.

Terms I–III, the components involving q_{net}, are shown in Fig. 10a. Term I, which represents the temperature tendency anomaly caused by anomalies in the net surface heat flux, is large throughout the year. While q'_{net} is largest during winter, so is $\bar{h}$ (Fig. 3a), the result is that term I is largest from May through October when it exceeds 0.5°C mo^{-1}. The second term makes a significant contribution to the development of positive SST′ during spring and summer. Physically, when the mixed layer shoals more than usual, the net surface heating is spread over a thinner layer increasing the temperature tendency. These results are consistent with the analyses of Elsberry and Garwood (1978) and Lanzante and Harnack (1983) who found that at OWS P when the mixed layer shoaled early relative to the norm, the summer SST was anomalously warm. Net surface heating causes a more buoyant and thus shal-

[3] Daily anomalies in h may not be small compared with the mean. The affects of this assumption on the monthly mean results are discussed later in this section.

lower mixed layer, which leads to a negative correlation between q'_{net} and h'. This results in a small but positive value of Term III over most months for both the positive and negative $\partial T'_m/\partial t$ composite, so term III enhances the development of warm SST anomalies and suppresses cold anomaly development.

Terms IV–VII, components which directly involve entrainment, are shown in Fig. 10b. All four terms have a pronounced seasonal cycle, with minimum values in winter as both W_e and ΔT are small, while $\bar{h}$ is large. From May through September term IV $[-(W'_e\overline{\Delta T}/\bar{h})]$, causes positive $\partial T'_m/\partial t$ as a reduced entrainment rate ($W'_e < 0$) brings in less cold water from below ($\bar{T}_m - \bar{T}_b = \overline{\Delta T} > 0$). Term V, which represents the mean entrainment of the anomalous temperature jump across h, has the largest values of the four entrainment terms and acts to strongly warm surface waters from August through November. These anomalies result from warmer than normal subsurface conditions ($\Delta T' < 0$), as $\bar{W}_e$ and $\bar{h}$ are always positive. Term VI, which is generally small, acts to enhance the rate of SST′ growth in October and November but damps it in August and September. Term VII damps $\partial T'_m/\partial t$ especially from May through October. When h' is negative, VII is also negative, as the mean cooling due to entrainment is contained within a thinner layer, and so this component tends to impede the growth of the SST anomaly.

The impact of entrainment on SST anomaly growth and the association between its components is complicated as a result of interrelationships between T_m, T_b, W_e, and h. If the temperature anomalies within the mixed layer were much larger than those in the layer below, then $\Delta T' > 0$, and Term V would act to damp SST anomalies. However, due to the storage of subsurface thermal anomalies (see section 5), T'_b can be large and uncorrelated with T'_m. As a result, the mean entrainment of these subsurface anomalies can cause SST anomalies to grow rapidly, especially in fall. The entrainment rate depends, in part, on the density jump at the base of the mixed layer; as $\Delta T'$ decreases so does the stability of the water column, leading to enhanced W_e. Thus, one would expect a negative correlation between $\Delta T'$ and W'_e and between terms IV and V as well. These two terms have opposite signs in 8 of the 12 months with the exception of March, and July through September (Fig. 10b). During late summer a decrease in wind stirring leads to $W'_e < 0$, but the supply of anomalously warm water below the surface maintains $\Delta T' < 0$, thus both terms IV and V can contribute to SST anomaly growth at times. The last three components of term VII depend on the relationship between entrainment and mixed layer depth, when $W'_e > 0$ so is h' as $W_e = dh/dt$, but recall that when h decreases, W_e is set to zero. Thus, over the course of a month, the correlation between W'_e and h' is not necessarily positive and depends upon the magnitude and frequency of shoaling.

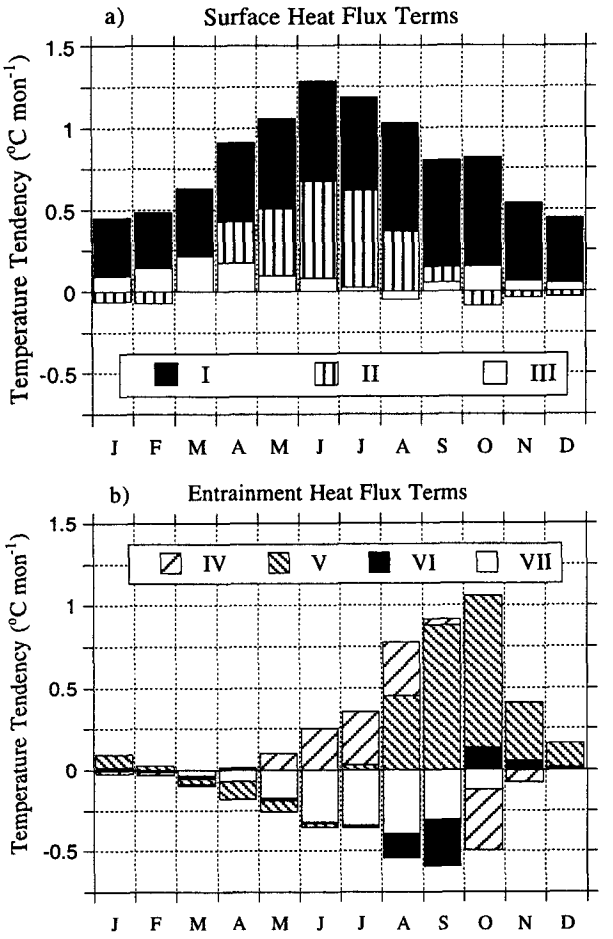

FIG. 10. The (a) surface and (b) entrainment heat flux terms (°C mo^{-1}) obtained from the decomposition of the SST tendency equation. The seven terms, derived from a composite of when the simulated monthly SST′ tendency exceeded one standard deviation, are given by (5).

Comparing the effects of the heating due to surface energy fluxes and entrainment, the sum of terms I–III and IV–VII, in Figs. 10a and 10b, respectively, indicates that q_{net} forcing of SST anomalies is important throughout the year while entrainment is important in the fall, in agreement with Alexander and Deser (1995). However, in decomposing the temperature tendency equation we assumed that $h' < \bar{h}$. This is a good approximation during most of the year except in summer and early fall when h' and $\bar{h}$ are of the same order of magnitude. As a result, the sum of terms IV–VII tends to slightly underestimate the positive contribution of the anomalous net entrainment heat flux, $(-W_e\Delta T/h)'$, to the growth of the SST′. The same is also true for the net surface heat flux.

The nonlinear equation that governs mixed layer depth [Eq. (50) in Gaspar 1988] is influenced by several processes including wind stirring, negative surface

buoyancy flux, and the density jump at the base of the mixed layer. These processes, represented by the friction velocity, $[u^* = (\tau/\rho_{air})^{3/2}]$, $-q_{net}$, and $-\Delta T(T_b - T_m)$, respectively, are then correlated with the monthly h values (Table 2). The anomaly correlation between all three variables and h, using all months of the 500-yr simulation, exhibits a pronounced seasonal cycle. The correlation between u^* and h is greatest from May through September when it exceeds 0.75. (Correlations between u^{*3}, which is used directly in the entrainment equation, and h exhibit a similar seasonal cycle as the $u^* - h$ correlations but were approximately $1/2$–$3/4$ as large.) In contrast, the correlation between $-q_{net}$ and h is a minimum in summer but exceeds 0.6 from January through April. While, in general, it is difficult to interpret cause and effect relationships using correlations, given that h has a limited influence on the surface heat and momentum fluxes, these large correlation values are indicative of the atmosphere forcing mixed layer depth anomalies.

Initially positive correlations were expected between h and $-\Delta T$, that is, the mixed layer depth would increase ($h' > 0$) when instability in the water column increased $[-\Delta T = (T_b - T_m)' > 0]$ and vice versa. The correlation between h and $-\Delta T$ is negative in January and February and from June through November. Other processes, such as wind stirring, could control h' and lead to negative correlations between h and $-\Delta T$. In addition, low or negative correlations between h and $-\Delta T$ can result from the decoupling between the two during shoaling, when h is computed from a balance between the surface mechanical and buoyancy forcing and is independent of ΔT. The correlations between W_e and $-\Delta T$ (not shown) are positive for all months except March and April, indicating that reducing the density jump at the base of the mixed layer does tend to increase h via entrainment.

The relationships between h and u^*, $-q_{net}$, and ΔT are not independent as the latter three variables are physically related to each other, for example, V is used in computing both u^* and $-q_{net}$, and $-q_{net}$ regulates T_m and thus ΔT. The linear part of this dependence can be removed using the method of partial correlations (e.g., Snedecor and Cochran 1980). The partial correlation values between u^* and h (Table 2), are slightly higher from May through July and lower over the remainder of the year compared with the correlations where the linear influence of $-q_{net}$ and $-\Delta T$ have not been removed. The partial correlations between h and $-q_{net}$ are positive for all 12 months, indicating that heat loss from the surface, which causes the surface water to sink, acts to deepen the mixed layer throughout the year. The partial correlations between h and $-\Delta T$ are relatively small, with absolute values of less than 0.3. Overall, the correlations in Table 2 indicate that wind mixing is the dominant term forcing mixed layer depth anomalies in summer, the surface buoyancy flux is most important in winter, while the stability of the water column, given by the jump in temperature at the base of the mixed layer, is of secondary importance throughout the year.

7. Summary and conclusions

A 500-yr simulation has been performed in which a stochastic model of atmospheric surface conditions in the northeast Pacific is used to drive an upper-ocean model. The atmospheric model, based on 30 years of data collected at OWS P, consists of three independent Markov models for the anomalous air temperature, wind speed, and solar radiation, while the dewpoint temperature anomaly mainly depends on T'_{air}. The spectral values of the atmospheric quantities provide a good fit to their observed counterparts at most frequencies. The stochastic anomalies are then added to the mean seasonal cycle of their respective fields and used in computing the boundary conditions for the bulk mixed layer model developed by Gaspar (1988). This stochastic/physical model is used to study air–sea interaction and upper-ocean processes.

TABLE 2. Correlations and partial correlations of the monthly mixed layer depth (h) with the upward net surface heat flux ($-q_{net}$), the friction velocity (u^*), and the temperature jump at the base of the mixed layer ($-\Delta T = (T_b - T_m)$).

	Month											
	Jan	Feb	Mar	Apr	May	Jun	Jul	Aug	Sep	Oct	Nov	Dec
						Correlations						
u^*	0.20	0.28	0.42	0.59	0.80	0.89	0.88	0.90	0.79	0.51	0.32	0.21
$-q_{net}$	0.66	0.77	0.83	0.61	0.15	−0.06	−0.17	−0.22	0.10	0.56	0.47	0.53
$-\Delta T$	−0.09	−0.29	0.05	0.56	0.21	−0.08	−0.04	−0.53	−0.58	−0.60	−0.28	0.11
						Partial correlation						
u^*	0.15	0.27	0.38	0.59	0.82	0.90	0.89	0.87	0.73	0.46	0.28	0.14
$-q_{net}$	0.68	0.75	0.83	0.26	0.09	0.22	0.20	0.30	0.42	0.51	0.40	0.55
$-\Delta T$	0.30	0.15	0.15	0.27	0.28	0.10	0.21	−0.04	−0.20	−0.27	−0.03	0.27

The ocean model realistically simulates both the mean and standard deviation of ocean temperatures over the seasonal cycle, though due to errors in the surface fluxes and model deficiencies it was necessary to apply a constant surface cooling of 16 W m^{-2} to obtain a reasonable mean state. The rms difference between the model and observations of the mean surface temperature for the 12 calendar months is ~0.25°C, compared to a seasonal cycle amplitude of ~3.5°C. However, the model underestimates the magnitude of the seasonal cycle especially below 100 m and the mixed layer shoals one to two months earlier than observed. Like the observations, the model exhibits maximum SST variability in the fall and a region of enhanced subsurface temperature variability in the summer seasonal thermocline, associated with fluctuations in the depth of the mixed layer depth (h). However, the model tends to underestimate the range of variability of both temperature and h over the course of the year.

The spectrum of the monthly SST anomalies from the 500-yr stochastic model run are in general agreement with observations, although the mixed layer model tends to slightly underestimate the variability at most periods. This suggests that neglected processes such as oceanic advection, covariability between the atmospheric forcing terms on monthly and longer timescales, and changes in surface forcing associated with ENSO contribute to SST variability in the northeast Pacific. To test the latter we performed an additional model simulation in which an approximation of the ENSO signal over the northeast Pacific was added to the stochastic forcing at OWS P. The results indicate that the low-frequency (periods > 2 years) response of the model's SST′ agreed better with observations when ENSO forcing is included.

The increase in SST variance with nearly the square of the period up to about a year and a flattening of the spectra at longer periods is consistent with the stochastic climate theory for midlatitude SST anomalies proposed by Frankignoul and Hasselmann (1977). The flattening of the spectra results from air–sea feedback and entrainment, which can be represented by linear damping, $-\lambda$ SST′. We estimate λ^{-1}, the decay constant, to be ~3 months in both the model and observations, which gave an excellent fit to the autocorrelation of SST anomalies out to approximately half a year, but overestimates the SST decay at longer lags. Linear stochastic theory appears to be valid on the timescales of less than ~6 months, even when the atmospheric forcing is not completely white (see Fig. 1a). If the mixed layer model acted as a simple integrator of T'_{air}, the resulting SST spectrum would be inversely proportional to a fourth-order polynomial in frequency. However, SST′ is forced by the net surface energy flux, which depends on a multiplication of T'_{air} with rapidly changing variables such as wind speed. The result is that q'_{net} varies rapidly (with a ~2 day decay time) and is nearly white on the timescales that SST varies.

A detailed analysis of the mixed layer temperature tendency has been performed to elucidate the role of surface and entrainment heat fluxes on SST anomalies. The anomalous net surface heat flux plays an important role in the growth of SST anomalies throughout the year and is the dominant term during winter. Entrainment of subsurface water into the mixed layer strongly influenced SST anomalies in fall, in agreement with Camp and Elsberry (1978) and Alexander and Deser (1995). Entrainment also influences the upper-ocean heat budget by controlling the depth of the mixed layer. Mixed layer depth anomalies are highly correlated with surface mechanical mixing in summer and surface buoyancy forcing in winter. Heat fluxes into the mixed layer are most effective in generating SST anomalies in late summer and early fall when the mixed layer is relatively shallow and thus has little thermal inertia. In addition, anomalies in h have a significant impact on the anomalous SST tendency during spring and summer. These results suggest that while a fixed slab representation of the upper ocean may be reasonable in winter, changes in h and the heat flux through the base of the mixed layer play an important role in the development of SST anomalies during the remainder of the year.

The seasonal cycle in mixed layer depth can also contribute to the recurrence of SST anomalies: anomalous warm or cold water created in the deep mixed layer during winter/spring can remain sequestered below the shallow mixed layer in summer and then be entrained into the surface layer in the following fall. Lead–lag correlations and composite analyses of the data indicate a clear connection between SST anomalies in spring and fall through the summer seasonal thermocline. This pattern also occurs in the model simulation but the connection to the surface in fall is less clear, and the pattern is more diffuse and extended over a longer portion of the seasonal cycle.

Given the importance of surface energy fluxes in forcing SST anomalies, the seasonal evolution of the ocean temperature anomalies clearly depends on the autocorrelation of surface flux anomalies. In addition, the close association between air temperature and SST, which strongly influences surface fluxes, makes it difficult to separate cause and effect relationships in the observed air–sea system. Hence, one must use caution when trying to confirm the re-emergence mechanism solely from observed ocean temperature data. Autocorrelations between monthly surface flux anomalies from the stochastic atmospheric model are near zero beyond 2 months lag (not shown); thus, aside from the slow decay of SST anomalies, seasonal lead–lag relationships between ocean thermal anomalies must result from other processes operating in the ocean model, primarily the re-emergence mechanism. A key feature of this mechanism appears to be the mean entrainment of

the anomalous difference in temperature between the water within and below the mixed layer ($\bar{W}_e \Delta T'/\bar{h}$), which dominates the surface heat budget during September and October (Fig. 10), where the temperature anomalies in the sub-mixed-layer water were created during the previous winter and spring. The ability of the stochastic/physical model of the air–sea system to obtain the signature of the re-emergence mechanism gives us greater confidence in its existence.

Here, we have studied upper-ocean variability using a relatively simple model at one location in the North Pacific driven by a statistical representation of surface atmospheric conditions. This model experiment gave similar results to a run in which the mixed layer ocean model was driven by observed atmospheric conditions at weathership P, suggesting that stochastic forcing can be an appropriate tool for studying aspects of the climate system. However, the results may be model and location dependent. So the ocean processes examined here, especially entrainment and the re-emergence mechanism, and the domain over which these processes are important, should be confirmed using additional observations and other models.

Acknowledgments. We thank Clara Deser, Joseph Barsugli, Matthew Newman, Shiling Peng, and two anonymous reviewers for their valuable comments. This work was supported by a Grant from the NOAA office of Global Programs.

APPENDIX

Stochastic Atmosphere Model Equations

a. Surface air temperature

Here, T'_{air} was modeled using a combination of two noninteracting linear Markov processes driven by white noise, $T'_{\text{air}} = T'_1 + T'_2$. The time evolution of T'_1 and T'_2 is given by

$$\frac{dT'_i}{dt} = B_i T'_i + \xi_i; \quad i = 1, 2, \tag{A1}$$

where the feedback parameter, B_i, corresponds to the inverse of the decay timescale of the system. The white noise forcing, ξ_i, is cyclostationary with respect to the seasonal cycle, and has variance $\langle \xi_i^2 \rangle dt = Q_i(t)$, where angle brackets indicate an ensemble average. We found the best fit to the observed spectrum by splitting the variability between the relatively slow system $i = 1$, which explains 75% of the variance and the faster system, $i = 2$, which explains the remaining 25%. A value of $B_1^{-1} = -28$ days, was obtained from the covariance properties of the observations, while selecting $B_2^{-1} = -2$ days, gave the best overall fit to the data.

Each of the two Markov processes obeys a fluctuation–dissipation relation (FDR: e.g., Penland and Matrosova 1994), which is essentially conservation of variance:

$$\frac{d\langle T_i'^2 \rangle}{dt} = 2B_i \langle T_i'^2 \rangle + Q_i(t); \quad i = 1, 2. \tag{A2}$$

Seasonally varying values of $Q_1(t)$ and $Q_2(t)$ were obtained from (A2) by using the 30 years of daily data to estimate $\langle T'^2_{\text{air}} \rangle$ and, hence, $\langle T_1'^2 \rangle$ and $\langle T_2'^2 \rangle$; the latter was chosen to be consistent with the observed spectra. Following Rümelin (1982), Kloeden and Platen (1992), and Penland and Matrosova (1994), T'_{air} was numerically generated using a forward time stepping scheme,

$$T'_{\text{air}}(t) = \sum_{i=1}^{2} T'_i(t) = \sum_{i=1}^{2} [T'_i(t - \delta) + B_i T'_i(t - \delta)\delta + \sqrt{Q_i(t - \delta)\delta} R_i], \tag{A3}$$

where δ is the time step and R_i a Gaussian random deviate with mean zero and unit variance.

b. Dewpoint temperature

Here, T'_{dew} is modeled as a linear regression on T'_{air}, plus a Gaussian random component added to account for the scatter around the regression line:

$$T'_{\text{dew}} = 0.12461 + 1.4135 T'_{\text{air}}(t) + \sqrt{1.3734} R. \tag{A4}$$

c. Shortwave radiation

Here, q'_{sw} is modeled using a single Markov process,

$$\frac{dq'_{\text{sw}}}{dt} = B_{\text{sw}}(t) q'_{\text{sw}} + \xi_{\text{sw}}; \quad \langle \xi_{\text{sw}}^2 \rangle dt = Q_{\text{sw}}(t), \tag{A5}$$

but B_{sw} in addition to Q_{sw} vary with the seasonal cycle, where $-B_{\text{sw}}^{-1}$ ranges between one and two days. As with T'_{air}, the variance of the stochastic forcing is obtained from the time-dependent FDR and a forward-stepping technique is used to calculate the synthetic time series of q'_{sw}.

d. Wind speed

The stochastic model for the time tendency of V' consists of a continuous, stable linear system driven by both multiplicative ($\xi_1 V'$) and additive (ξ_2) stochastic forcing; that is,

$$\frac{dV'}{dt} = B_v V' + \xi_1 V' + \xi_2, \tag{A6}$$

where $\langle \xi_1^2 \rangle dt = Q_{v1}$, and $\langle \xi_2^2 \rangle dt = Q_{v2}$. Including multiplicative forcing influences the decay time of the system as seen from the lagged autocorrelation function for V' with lag τ:

$$\langle V''(t + \tau) V'(t) \rangle = \exp\left[\left(B_V + \frac{1}{2} Q_{V1} \right) \tau \right] \langle V'^2 \rangle \equiv \exp(B_V^* \tau) \langle V'^2 \rangle, \tag{A7}$$

for small τ. Since B_V is negative, while Q_{V_1} is necessarily positive, the effect of the "noise-induced drift" $\frac{1}{2}Q_{V_1}$) due to the multiplicative noise is to *increase* the decay time. It is not B_V but rather B_V^* that is obtained from the observed covariance properties of V'. Further, the FDR is

$$\frac{d\langle V'^2\rangle}{dt} = 2B_V^*\langle V'^2\rangle + Q_{V_1}\langle V'^2\rangle + Q_{V_2} \quad \text{(A8a)}$$

$$= 2(B_V + Q_{V_1})\langle V'^2\rangle + Q_{V_2}. \quad \text{(A8b)}$$

The effective decay time $-B_v^* - 1$ varies daily from approximately 1.3 days in winter to 2.5 days in summer. The additive noise, obtained from [Eq. (A8)] and consideration of the observed spectrum, contains 92.5% of the total noise variance, while the multiplicative noise accounts for the remaining 7.5%.

The forward-stepping technique used to integrate [Eq. (A6)] does not include the effect of the noise-induced drift (Rümelin 1982). Rather than use the more complicated Runge–Kutta method, we compensated for the deficiency in the forward-stepping technique by adjusting the deterministic part of the equation; that is, B_V was replaced by B_V^*:

$$V'(t) = V'(t - \delta) + B_V^*V'(t - \delta)\delta + \sqrt{Q_{V_1}\delta}V'(t - \delta)R_1 + \sqrt{Q_{V_2}\delta}R_2. \quad \text{(A9)}$$

The probability distribution of the wind anomalies generated by this model is symmetric. However, the total wind speed, the anomaly plus the climatological value, is not allowed to exceed 50 m s^{-1} or fall below 1 m s^{-1}. These restrictions introduced a slight skew in the wind speed distribution (not shown), which also occurs in the observations.

REFERENCES

Adamec, D., R. L. Elsberry, R. W. Garwood, and R. L. Haney, 1981: An embedded mixed-layer-ocean circulation model. *Dyn. Atmos. Oceans,* **6,** 69–96.

Alexander, M. A., 1990: Simulation of the response of the North Pacific Ocean to the anomalous atmospheric circulation associated with El Niño. *Climate Dyn.,* **5,** 53–65.

——, 1992: Midlatitude atmosphere–ocean interaction during El Niño. Part I: The North Pacific Ocean. *J. Climate,* **5,** 944–958.

——, and C. Deser, 1995: A mechanism for the recurrence of wintertime midlatitude SST anomalies. *J. Phys. Oceanogr.,* **25,** 122–137.

——, and C. Penland, 1995: Variability in a mixed layer model of the upper ocean driven by stochastic atmospheric surface fluxes. *Proc. of the 19th Annual Climate Diagnostics Workshop,* College Park, MD, NOAA, 365–368.

Battisti, D. S., U. S. Bhatt, and M. A. Alexander, 1995: A modeling study of the interannual variability in the wintertime North Atlantic Ocean. *J. Climate,* **8,** 3067–3083.

Bjerknes, J., 1969: Atmospheric teleconnections from the equatorial Pacific. *Mon. Wea. Rev.,* **97,** 163–172.

Blackmon, M. L., J. E. Geisler, and E. J. Pitcher, 1983: A general circulation model study of January climate anomaly patterns associated with interannual variation of equatorial Pacific sea surface temperatures. *J. Atmos. Sci.,* **40,** 1410–1425.

Camp, N. T., and R. L. Elsberry, 1978: Oceanic thermal response to strong atmospheric forcing. Part II: The role of one-dimensional processes. *J. Phys. Oceanogr.,* **8,** 215–224.

Delworth, T., S. Manabe, and R. J. Stouffer, 1993: Interdecadal variations of the thermohaline circulation in a coupled ocean–atmosphere model. *J. Climate,* **6,** 1993–2011.

Deser, C., and M. L. Blackmon, 1993: Surface climate variations over the North Atlantic Ocean during winter: 1900–89. *J. Climate,* **6,** 1743–1753.

——, M. A. Alexander, and M. S. Timlin, 1996: Upper-ocean thermal variations in the North Pacific during 1970–1991. *J. Climate,* **9,** 1840–1855.

Elsberry, R., and R. W. Garwood, 1978: Sea surface temperature anomaly generation in relation to atmospheric storms. *Bull. Amer. Meteor. Soc.,* **59,** 786–789.

Emery, W. J., and K. Hamilton, 1985: Atmospheric forcing of interannual variability in the northeast Pacific Ocean: Connections with El Niño. *J. Geophys. Res.,* **90,** 857–868.

Farrell, B., and P. J. Ioannou, 1993: Stochastic dynamics of baroclinic waves. *J. Atmos. Sci.,* **50,** 4044–4057.

Fissel, D., S. Pond, and M. Miyake, 1976: Spectra of surface atmospheric quantities at Ocean Weathership P. *Atmosphere,* **14,** 77–97.

Frankignoul, C., 1979: Stochastic forcing models of climate variability. *Dyn. Atmos. Oceans,* **3,** 465–479.

——, 1985: Sea surface temperature anomalies, planetary waves, and air–sea feedback in the middle latitudes. *Rev. Geophys.,* **23,** 357–390.

——, and K. Hasselmann, 1977: Stochastic climate models. Part 2. Application to sea-surface temperature variability and thermocline variability. *Tellus,* **29,** 284–305.

——, and R. W. Reynolds, 1983: Testing a dynamical model for midlatitude sea surface temperature anomalies. *J. Phys. Oceanogr.,* **13,** 1131–1145.

Gaspar, P., 1988: Modeling the seasonal cycle of the upper ocean. *J. Phys. Oceanogr.,* **18,** 161–180.

Gill, A. E., 1979: Comments on stochastic models of climate variability. *Dyn. Atmos. Oceans,* **3,** 481–483.

——, 1982: *Atmosphere–Ocean Dynamics.* Academic Press, 662 pp.

Griffies, S. M., and E. Tziperman, 1995: A linear thermohaline oscillator driven by stochastic atmospheric forcing. *J. Climate,* **8,** 2440–2453.

Haney, R. L., and R. W. Davies, 1976: The role of surface mixing in the seasonal variation of the ocean thermal structure. *J. Phys. Oceanogr.,* **6,** 504–510.

Hartmann, D. L., 1974: Time spectral analysis of midlatitude disturbances. *Mon. Wea. Rev.,* **102,** 348–362.

Hasselmann, K., 1976: Stochastic climate models. *Tellus,* **28,** 473–485.

Isemer, H. J., and L. Hasse, 1987: *Air–Sea Interactions.* Vol. 2, *The Bunker Climatic Atlas of the North Atlantic,* Springer-Verlag, 252 pp.

Jacobs, G. A., H. E. Hurlburt, J. C. Kindle, E. J. Metzger, J. L. Mitchell, and A. J. Wallcraft, 1994: Decade-scale trans-Pacific propagation and warming effects of an El Niño anomaly. *Nature,* **370,** 360–363.

Kloeden, P., and E. Platen, 1992: *Numerical Solution of Stochastic Differential Equations.* Springer-Verlag, 632 pp.

Kraus, E. B., and J. A. Businger, 1994: *Atmosphere–Ocean Interaction.* 2d ed. Oxford University Press, 362 pp.

Kushnir, Y., 1994: Interdecadal variations in North Atlantic sea surface temperature and associated atmospheric conditions. *J. Climate,* **7,** 141–157.

Lanzante, J. R., and R. P. Harnack, 1983: An investigation of summer sea surface temperature anomalies in the eastern North Pacific Ocean. *Tellus,* **35A,** 256–268.

Large, W. G., and S. Pond, 1982: Sensible and latent heat flux measurements over the oceans. *J. Phys. Oceanogr.,* **12,** 464–482.

——, J. C. McWilliams, and P. P. Niiler, 1986: Upper ocean thermal response to strong autumnal forcing over the Northeast Pacific. *J. Phys. Oceanogr.,* **16,** 1524–1550.

Large, W. C., J. C. McWilliams, and S. C. Doney, 1994: Oceanic vertical mixing: A review and a model with a nonlocal boundary layer parameterization. *Rev. Geophys.,* **32,** 363–404.

Latif, M., and T. P. Barnett, 1994: Causes of decadal climate variability over the North Pacific and North America. *Science,* **266,** 634–637.

Lau, K. M., 1985: Elements of stochastic-dynamical theory of the long term variability of El Niño/Southern Oscillation. *J. Atmos. Sci.,* **42,** 1552–1558.

Lau, N.-C., and M. J. Nath, 1996: The role of the "atmospheric bridge" in linking tropical Pacific ENSO events to extratropical SST anomalies. *J. Climate,* **9,** 2036–2057.

Levitus, S., 1982: *Climatological Atlas of the World Ocean.* NOAA Prof. Paper No. 13, U.S. Govt. Printing Office, 173 pp.

Manabe, S., and R. J. Stouffer, 1988: Two stable equilibria of a coupled ocean–atmosphere model. *J. Climate,* **1,** 841–866.

Martin, P. J., 1985: Simulation of the mixed layers at OWS November and Papa with several models. *J. Geophys. Res.,* **90,** 903–916.

Mikolajewicz, U., and E. Maier-Reimer, 1990: Internal secular variability in an ocean general circulation model. *Climate Dyn.,* **4,** 145–156.

Mitchell, J. M., Jr., 1976: An overview of climate variability and its causal mechanisms. *J. Quat. Res. N.Y.,* **6,** 481–493.

Miyakoda, K., and A. Rosati, 1984: The variation of sea surface temperature in 1976 and 1977 2. The simulation with mixed layer models. *J. Geophys. Res.,* **89,** 6533–6542.

Namias, J., and R. M. Born, 1970: Temporal coherence in North Pacific sea-surface temperature patterns. *J. Geophys. Res.,* **75,** 5952–5955.

——, and ——, 1974: Further studies of temporal coherence in North Pacific sea surface temperatures. *J. Geophys. Res.,* **79,** 797–798.

Paulson, C. A., and J. J. Simpson, 1977: Irradience measurements in the upper ocean. *J. Phys. Oceanogr.,* **7,** 952–956.

Payne, R. E., 1972: Albedo of the sea surface. *J. Atmos. Sci.,* **29,** 959–970.

Penland, C., 1996: A stochastic model of IndoPacific sea surface temperature anomalies. *Physica D,* in press.

——, and L. Matrosova, 1994: A balance condition for stochastic numerical models with application to the El Niño–Southern Oscillation. *J. Climate,* **7,** 1352–1372.

——, and P. D. Sardeshmukh, 1995: The optimal growth of tropical sea surface temperature anomalies. *J. Climate,* **8,** 1999–2024.

Price, J. F., C. N. K. Mooers, and J. C. v. Leer, 1978: Observation and simulation of storm-induced mixed-layer deepening. *J. Phys. Oceanogr.,* **8,** 582–599.

Preisendorfer, R. W., 1988: *Developments in Atmospheric Science.* Vol. 17, *Principal Component Analysis in Meteorology and Oceanography,* Elsevier, 425 pp.

Reed, R. K., 1977: On estimating insolation over the ocean. *J. Phys. Oceanogr.,* **17,** 401–404.

Reynolds, R. W., 1978: Sea surface temperature anomalies in the North Pacific Ocean. *Tellus,* **30,** 97–103.

Rümelin, W., 1982: Numerical treatment of stochastic differential equations. *SIAM J. Numer. Anal.,* **19,** 604–613.

Slepian, D., 1983: Some comments in Fourier analysis, uncertainty and modeling. *SIAM Rev.,* **25,** 379–393.

Snedecor, G. W., and W. G. Cochran, 1980: *Statistical Methods.* The Iowa State University Press, 507 pp.

Sausen, R., K. Barthel, and K. Hasselmann, 1988: Coupled ocean–atmosphere models with flux correction. *Climate Dyn.,* **2,** 145–163.

Tabata, S., 1965: Variability of oceanographic conditions at Ocean Station "P" in the northeast Pacific Ocean. *Trans. Symp. Time Series Measurements in Oceanography,* Vol. 3, Ser. IV, Roy. Soc. Can., 367–418.

Thomson, D. J., 1982: Spectrum estimation and harmonic analysis. *Proc. IEEE,* **70,** 1055–1096.

——, 1990: Quadratic-inverse spectrum estimates: Applications to paleoclimatology. *Philos. Trans. Roy. Soc. London A,* **332,** 539–597.

Trenberth, K. E., 1996: The 1990–95 El Nino–Southern Oscillation event: Longest on record. *Geophys. Res. Lett.,* **23,** 57–60.

——, and J. W. Hurrell, 1994: Decadal atmosphere–ocean variations in the Pacific. *Climate Dyn.,* **9,** 303–319.

Vautard, R., P. Yiou, and M. Ghil, 1992: Singular-spectrum analysis: A toolkit for short, noisy, chaotic signals. *Physica D,* **58,** 95–126.

Weaver, A. J., and E. S. Sarachik, 1991: Evidence for decadal variability in an ocean general circulation model: An advective mechanism. *Atmos.-Ocean,* **29,** 197–231.

White, W., and R. Bernstein, 1981: Large-scale vertical eddy diffusion in the main pycnocline of the central North Pacific. *J. Phys. Oceanogr.,* **11,** 434–441.

Woods, J. D., and W. Barkmann, 1986: The response of the upper ocean to solar heating. Part I: The mixed layer. *Quart. J. Roy. Meteor. Soc.,* **112,** 1–27.

Wunsch, C., 1992: Decade-to-century changes in the ocean circulation. *Oceanography,* **5,** 99–106.

Yan, X.-H., and A. Okubo, 1992: Three-dimensional analytical model for the mixed layer depth. *J. Geophys. Res.,* **97,** 20 201–20 226.

Yiou, P., and Coauthors, 1991: High-frequency paleovariability in Climate and CO_2 levels from Vlostok ice core records. *J. Geophys. Res.,* **96,** 20 365–20 378.